Received 22 December 2023; revised 18 April 2024; accepted 4 June 2024.
Date of publication 10 June 2024; date of current version 19 June 2024.

Digital Object Identifier 10.1109/OJUFFC.2024.3411578

Sound Speed and Virtual Source Correction in Synthetic Transmit Focusing

ANDERS EMIL VRÅLSTAD[1] (Graduate Student Member, IEEE), OLE MARIUS HOEL RINDAL[2] (Member, IEEE), TORE GRÜNER BJÅSTAD[3] (Member, IEEE), AND SVEIN-ERIK MÅSØY[1]

[1]Department of Circulation and Medical Imaging, Norwegian University of Science and Technology (NTNU), 7491 Trondheim, Norway
[2]Department of Informatics, University of Oslo, 0316 Oslo, Norway
[3]GE Vingmed Ultrasound AS, 3183 Horten, Norway

CORRESPONDING AUTHOR: A. E. VRÅLSTAD (anders.e.vralstad@ntnu.no)

This work was supported in part by the Center for Innovative Ultrasound Solutions (CIUS) and in part by the Research Council of Norway under Project 237887.

ABSTRACT In beamforming, retrospective change in sound speed and recalculation of focusing delays is attractive both for improving image quality and for using it in an iterative image quality optimization process. Modifying the speed of sound retrospectively for focused transmits is challenging because the transmit focus position is a function of sound speed error. The virtual source model is a common way to calculate the transmit focusing delays where using the correct transmit focus position is imperative. In this paper, we provide the methods necessary to perform a retrospective sound-speed correction by compensating the receive grid and by calculating the effective transmit focus needed to perform proper synthetic transmit focusing. To evaluate the efficacy of our method, we simulate wave propagation and measure the resolution of *in vitro* images using both phased and curvilinear arrays. The results of the suggested virtual source estimation method match the simulated wave propagation for multiple F-numbers and both positive and negative sound speed errors. We compare beamformed images using correct/incorrect sound speeds and correct/incorrect virtual source positions. The results demonstrate that the Corrected Virtual Source (CVS) method generates artifact-free images with superior quality compared to images with incorrect sound speed. Furthermore, the image beamformed with the correct sound speed, but incorrect virtual source position, exhibits image artifacts and inferior focusing quality compared to the CVS image.

INDEX TERMS Image quality, retrospective beamforming, virtual source, speed of sound.

I. INTRODUCTION

THE speed of sound of human tissue is approximated to be 1540 m/s and homogeneous for conventional ultrasound imaging systems [1]. If the tissue speed of sound deviates from the estimated mean value, this results in poorer image quality. As an example, the sound speed of fat is approximated to be 1450 m/s [2].

Multiple methods have been proposed to estimate the global speed of sound in medical ultrasound. A literature review on this topic and other aberration correction methods was recently published by Ali et al. [3]. Some research suggests a direct estimate using the phase distribution across the aperture [4], [5] or using a tomographic registration of images from steered transmit events [6].

Several researchers suggest optimizing an image quality metric by beamforming using multiple speed of sound values [7], [8], [9], [10], [11], [12]. This process may be repeated, iterated, until the desired convergence criterion is met. One way of achieving this is to iterate towards the correct sound speed by transmitting repeatedly with an updated sound speed estimate and using the image quality metric as a convergence criterion [8], [9], [10]. Such a method would not be practical for real-time imaging because of the required multiple transmissions. A potentially faster approach is instead to do this retrospectively with synthetic transmit and receive focusing using the same received signals.

This retrospective approach is used by others for Synthetic Transmit Aperture Imaging (STAI) and plane wave

acquisitions [11], [13]. This paper provides the necessary methods to perform retrospective sound speed correction for focused transmissions and other sequences using a virtual source. The virtual source is most commonly used to model a focused transmit event, but the model also supports synthetic aperture, diverging, and plane wave transmissions [14], [15], [16], [17], [18]. The key concept of the virtual source model is to calculate the Time-Of-Flight (TOF) curvature as if a spherical wave were propagating from a point in virtual medium with an assumed sound speed. For focused transmits, the source is positioned in the transmit focus, and the assumed sound speed of the virtual medium is what is assumed on transmit. The TOF model is valid within the transmitted beam field of view, modeled as two triangles with vertices at the focus position as shown by the solid blue lines in Fig. 3.

We do not specify the procedure of choosing the new sound speed needed for calculating the correct time-of-flight, as this can vary for different estimation approaches. Examples of such estimation approaches are brute-force methods, beamforming multiple images with sound speeds within an interval [9], [10], [11], and iterative methods choosing the next sound speed iteratively [7], [8], [12].

The aperture apodization and delays used in transmit beamforming determine the acoustic field excited in the object to be imaged. On receive, the delay-and-sum process should ideally process the received channel data in a manner that gives optimal focusing. Academic and industrial research on the topics of Synthetic Transmit Focusing (STF) has led to the technique called Retrospective Transmit Beamforming (RTB) [19]. RTB combines multiple transmit events in every beamformed image pixel, which synthesizes transmit focusing retrospectively. An alternative to RTB is REFoCUS beamforming, which converts received signals from an arbitrary scan sequence into a synthetic aperture dataset and performs synthetic aperture focusing [20], [21]. The two methods have shown an approximately equivalent synthetic transmit focusing quality [22]. In this paper, we investigate RTB. The two parts of synthetic beamforming, Dynamic Receive Focusing (DRF) and RTB, calculate TOF values assuming wave propagation models. DRF assumes a spherical wave that originates from the imaging point of interest. A common approach for calculating the TOF with RTB is to use a virtual source delay model.

We propose a method to estimate the effective virtual source position to be used in RTB when the sound speed is retrospectively changed. The Corrected Virtual Source (CVS) method can be applied as part of a sound speed estimation procedure using RTB. In such a procedure, images are reconstructed for a range of sound speeds and an estimate found by optimizing a defined image quality metric, *e.g.* pixel brightness or coherence [23]. The CVS method is general and may be applied to a variety of probe geometries and pulse sequences. Focused transmissions from a phased and curvilinear array (assuming no steering for the curvilinear case) are investigated in detail.

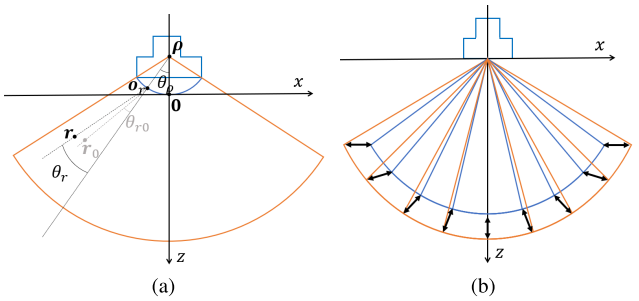

FIGURE 1. (a) A curvilinear array with an example of how a pixel position changes, from $\mathbf{r_0}$ to r, when there is a difference in sound speed in Tx and Rx beamforming. The vector positions are given with reference to the origin of the coordinate system $\mathbf{0} = [0, 0, 0]^T$. (b) Illustration of how the receive grid sector is deformed for a flat phased array. The receive grid is reduced when beamforming with a sound speed c higher than the sound speed assumed during transmission c_0 and enlarged when $c < c_0$.

We also propose a method for compensating the scan grid, which enables pixel-to-pixel comparison of images beamformed with different sound speeds retrospectively. Compensation is important when retrospectively comparing image quality between images beamformed with different sound speeds [13]. This is because image quality metrics are a function of the imaging object and changing the sound speed without grid compensation may move some part of the object out of the image scene.

The theory of this work is presented in Section II. A one-way transmit beam TOF simulation study is performed as described in Section III-B and its results are given in Section IV-A. The methodology for evaluating the focus quality of point targets is described in Section III-C. To validate the estimated virtual source positions when changing the sound speed retrospectively, we image point targets of a phantom with known sound speed and correct the sound speed retrospectively. The results are presented in Section IV-B. A discussion of the results and proposals for further extensions of the work is provided in Section V with a conclusion in Section VI.

II. THEORY

This paper uses bold notation for 3D euclidean vectors (*e.g.* $\boldsymbol{\xi} = \left[\xi_x, \xi_y, \xi_z\right]^T$) and scalar values without bold notation (*e.g.* ξ).

A. SCAN GRID COMPENSATION

The assumed positions of the imaged pixels $\mathbf{r}_0$ change to position $\mathbf{r}$ when the speed of sound is different during Tx and Rx beamforming (see Fig. 1).

The effective 2D scan grid can be calculated by defining the assumed pixel positions using scanlines with linearly increasing depth $\|\mathbf{r}_0 - \mathbf{o}_r\|$, steering angle θ_{r0}, and starting at the origin of the receive beam $\mathbf{o}_r$. Fig. 1a visualizes the vectors that define the scan grid and also shows an example

of how the assumed pixel position $\mathbf{r}_0$ is changed to $\mathbf{r}$ when a new sound speed c, different from c_0, is retrospectively assumed. The steering angle θ_r is defined as the angle deviation from θ_ρ, which is the normal vector of the active probe aperture evaluated at the receive beam origin position $\mathbf{o}_r$. The origins of a stepped scan/walking aperture acquisition will move with the active transmit aperture. Fig. 1b visualizes how the full scan grid is changed for a phased array. A phased array acquisition has all scanlines originating from the same origin, positioned at the center of the array ($\mathbf{o}_r = \mathbf{0}$ and $\theta_\rho = 0$). The geometry change of pixel depth is a simple scaling by the sound speed ratio starting at the receive beam origin, given as

$$\|\mathbf{r} - \mathbf{o}_r\| = \frac{c}{c_0}\|\mathbf{r}_0 - \mathbf{o}_r\|. \tag{1}$$

The change of angle is given by Snell-Descartes law of refraction [24],

$$\frac{\sin\theta_0}{c_0} = \frac{\sin\theta}{c}, \tag{2}$$

which is used to express the new pixel angle as

$$\theta_r = \arcsin\left(\frac{c}{c_0}\sin(\theta_{r0})\right), \tag{3}$$

in the case where the sound speed c_0 was assumed on Tx beamforming and c was used on Rx beamforming. By transforming the grid using (1) and (3) before performing pixel based beamforming, explained in Section II-II-C, the same received signals can be beamformed using different sound speed values and keeping image structures stationary. The proposed pixel-grid transformation is similar to the compensation for plane waves and flat phased array by Strohm et al. in [13]. The transformation facilitates pixel-to-pixel image quality comparison and is important when using an image quality metric to evaluate beamforming performance. This is because most image quality metrics are dependent on the imaged object. In order to accurately assess the image quality metrics on a pixel-by-pixel basis, it is necessary for the object being imaged to remain in the same place in the image for different trial sound speeds. In this way, it is only the focusing quality that is changed and not the spatial mapping of structures. The spatial axes in this paper are given in number of wavelengths because the conventional spatial coordinates assume a sound speed. That is, we first transform to the assumed Tx grid (using c_0) and then plot the axes in number of wavelengths.

B. TIME-OF-FLIGHT (TOF)

The coordinate system for a stepped curvilinear scan with a focused transmit wave is shown in Fig. 2. The figure shows the geometry of the array for a single transmit event with active transmit aperture center $\mathbf{o}$, focus point $\mathbf{v}$, element position $\mathbf{e}$ and center of curvature $\boldsymbol{\rho}$. The figure and further expressions are generalized to a flat phased array by taking the limit when the Radius Of Curvature (ROC) $\|\boldsymbol{\rho}\|$ approaches infinity. Note that there is a difference between the transmit origin angle θ_ρ and the steering angle θ.

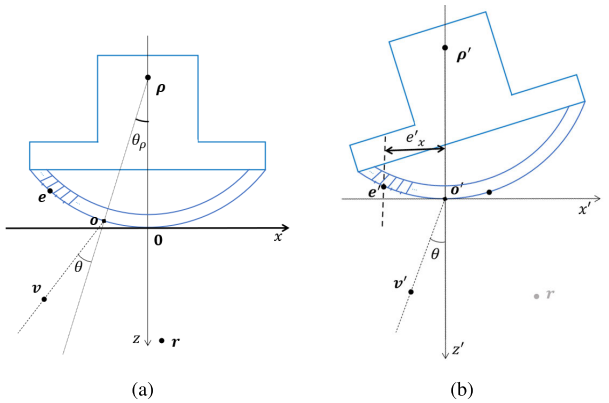

FIGURE 2. (a) 1D array geometry for single focused transmit event on a curvilinear array. Bold notation correspond to euclidean coordinates. Vector positions are given in reference to the coordinate system origin 0 = [0, 0, 0]^T. (b) Linearly transformed coordinate system according to the transformation in (8). Bold notation with { ′ } correspond to the transformed euclidean coordinates.

The TOF calculation for a pixel $\mathbf{r}$ can be divided into a transmit TOF t_{Tx} and a receive TOF t_{Rx}. The receive TOF t_{Rx} (DRF) is given as

$$t_{\mathrm{Rx}}(\mathbf{r}, \mathbf{e}) = \frac{\|\mathbf{r} - \mathbf{e}\|}{c}, \tag{4}$$

where $\mathbf{e}$ is the element position, $\mathbf{r}$ the compensated pixel position and c the sound speed. The transmit TOF t_{Tx} is given as

$$t_{\mathrm{Tx}}(\mathbf{r}, \mathbf{v}) = \frac{\|\mathbf{v}\| \pm \|\mathbf{r} - \mathbf{v}\|}{c} - t_0, \tag{5}$$

where the $\mathbf{v}$ is the virtual source position, and the time t starts when the wavefront is excited from the active transmit aperture center $\mathbf{o}$, and t_0 is the time when the transmitted wavefront passes the origin of the full array, which we also define as the origin of the coordinate system, $\mathbf{0} = [0, 0, 0]^T$ in Fig. 2. The sign in front of the $\|\mathbf{r}-\mathbf{v}\|$ term in (4) is positive if the position of the pixel $\mathbf{r}$ is deeper than that of the virtual source $\mathbf{v}$ and negative otherwise [15].

The refraction caused by the difference in sound speed at the array-medium interface, results in a wave propagating with a curvature focusing at a different virtual source position than what is assumed. In order to perform synthetic transmit focusing properly, the virtual source position needs to be compensated for. The updated virtual source position is found by solving the equations derived in Section II-E.

C. PIXEL-BASED ARRAY BEAMFORMING

The Delay-And-Sum (DAS) beamformer is implemented using TOF models from (5) and (4) as expressed in

$$b(\mathbf{r}) = \sum_{n=1}^{N}\sum_{k=1}^{K} w(n,k,\mathbf{r})\, s(n,k,t)\, e^{i2\pi f_{\mathrm{demod}} t}, \tag{6}$$

where

$$t = t_{\mathrm{Tx}}(\mathbf{r}, \mathbf{v}_k) + t_{\mathrm{Rx}}(\mathbf{r}, \mathbf{e}_n), \tag{7}$$

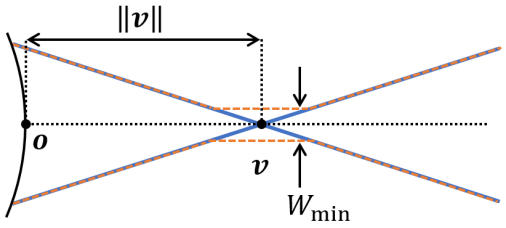

FIGURE 3. Geometric beam weighting as a function of virtual source position v and a minimum beam width W_{min}.

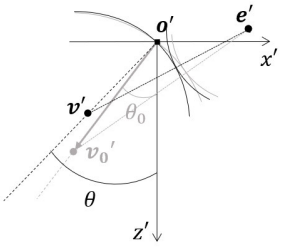

FIGURE 4. Example illustration of a virtual source position change due to a wrong sound speed assumption for a single transmit element e′. The assumed virtual source is shown with subscript 0 in gray color and the effective virtual source is shown in black color.

and N is the number of receive elements, K is the number of transmitted pulse sequences, $s(n, k, t)$ is the In-Quadrature (IQ) channel data signal up mixed by the exponential term where f_{demod} is the demodulation frequency, and $w(n, k, \mathbf{r})$ is the apodization weighting for element directivity, expanding aperture and transmit beam geometry weighting. The weighting of the beam geometry is a function of the virtual source position as illustrated in Fig. 3.

The beamformer in (6) performs both RTB and DRF by coherently compounding all transmits (K) and receivers (N) into the same coordinate grid.

D. COORDINATE SYSTEM TRANSFORMATION

In order to simplify further derivations, all vectors are linearly shifted with $\boldsymbol{\rho}$ and rotated with $R(\theta_\rho)$. This is a rotation around the point $\boldsymbol{\rho}$ and is expressed as

$$\begin{aligned}\boldsymbol{\xi}' &= R(\theta_\rho) \times (\boldsymbol{\xi} - \boldsymbol{\rho}) + \boldsymbol{\rho} \\ &= \begin{pmatrix} \cos\theta_\rho & 0 & -\sin\theta_\rho \\ 0 & 1 & 0 \\ \sin\theta_\rho & 0 & \cos\theta_\rho \end{pmatrix} \times (\boldsymbol{\xi} - \boldsymbol{\rho}) + \boldsymbol{\rho}, \end{aligned} \tag{8}$$

where $\{\times\}$ indicate matrix multiplication, $\boldsymbol{\xi}$ represents an arbitrary 3D vector and θ_ρ is the angle of the probe surface normal vector in the transmit origin relative to the z-axis as shown in Fig. 2a. The resulting coordinate system is visualized in Fig. 2b.

For a flat phased array this is the identity matrix and no shift because $\theta_\rho = 0 \Rightarrow R(\theta_\rho) = \not\Vdash \Rightarrow \boldsymbol{\xi}' = \boldsymbol{\xi}$.

E. SPEED-OF-SOUND CORRECTION of VIRTUAL SOURCE

When the assumption of speed of sound c_0 matches the speed of sound in the imaging medium c_m, the wave will approximate a circular wavefront with a single focus point at depth $\|\mathbf{v}_0\|$ with steering angle θ_0. However, when the speed of sound in the medium is different from that assumed, the wavefront will propagate in a new azimuth direction and will not converge at a singular depth but at a distribution of depths [25]. Fig. 4 shows an example of virtual source relocation due to the wrong sound speed assumption for one element position $\mathbf{e}'$. The relocation will vary for different elements.

To calculate the change in virtual source position given an estimated speed of sound c, we investigate the refraction at the array-medium boundary, and approximate the refracted wave using the same virtual source model. Equations (9)-(11) and (12), as shown at the bottom of the next page, express this algebraically for a 2D scan and a 1D probe, where $\mathbf{v}_0'$ and $\mathbf{v}'$ are the assumed and new virtual source positions, respectively. This is geometrically interpreted as finding the circle that intersects the origin $\mathbf{o}'$ and tangents the wavefront at $t = 0$ as shown in Fig. 4.

We assume here that both the assumed speed of sound used on Tx c_0 and the new speed of sound c are known in order to estimate the updated virtual source position. In an iterative image quality optimization scheme, c can be thought of as the estimate (it may also simply be guessed) of the optimal sound speed of the medium c_m. Optimal image quality will be obtained when $c = c_m$ because this produces the correct DRF TOF and RTB TOF.

In the derivation, we start by equating the initial boundary conditions, which are the excitation delays over the array boundary. For each virtual source position we solve the equation

$$\tau(\mathbf{v}_0', c_0) = \tau(\mathbf{v}', c) \tag{9}$$

$$\iff \tau(\mathbf{v}_0', c_0) = \frac{\|\mathbf{v}'\| - \|\mathbf{v}' - \mathbf{e}'\|}{c}. \tag{10}$$

By assuming a 1D array ($e_y' = o_y' = v_y' = 0$) and inserting polar coordinates ($\mathbf{v}' = \left[v_x', 0, v_z'\right]^T = \left[\|\mathbf{v}'\| \sin\theta, 0, \|\mathbf{v}'\| \cos\theta\right]^T$) we can further express this relation as

$$\tau(\mathbf{v}_0', c_0) = \frac{\|\mathbf{v}'\| - \sqrt{(\|\mathbf{v}'\| \sin\theta - e_x')^2 + (\|\mathbf{v}'\| \cos\theta - e_z')^2}}{c}. \tag{11}$$

We further constrain the solutions to (11) by determining the azimuth angle θ of the focus point from the assumed angle θ_0 using Snell-Descartes law of refraction (2). Inserting (2) into (11) gives an equation with only one unknown variable $\|\mathbf{v}'\|$, as expressed in (12). This equation can be solved numerically using the numerical root finding algorithm Fixed Point Iteration (FPI) [26]. The FPI assumes an initial solution and iterates on the solution using the expression in (13), as shown at the bottom of the next page. For a phased array with

$e'_z = 0$ we simplify (13) to

$$\|\mathbf{v}'\|_{i+1} = c\tau(\mathbf{v}'_0, c_0) + \sqrt{\|\mathbf{v}'\|_i^2 - 2\|\mathbf{v}'\|_i e'_x \frac{c}{c_0}\sin\theta_0 + e'^2_x}\,. \tag{14}$$

By investigating (12) for a flat ($e'_z = 0$) array at high F-numbers (Fraunhofer approximation with $\|\mathbf{v}'\| \gg |e_x|$) we obtain the relation

$$\|\mathbf{v}'\| = \frac{c_0}{c}\|\mathbf{v}'_0\|. \tag{15}$$

This is similar to the relation published in [25] and [27] and can be used when the approximations holds or as an initial solution in the FPI.

Because the steering angles of both the receive pixels (Rx beams) and the virtual sources (Tx beams) are modified by the change in sound speed, only correcting one-way will make the transmit and receive beams not align. This can create skewness artifacts by steering the sidelobe into the mainlobe of the other. For a curvilinear setup with no steering ($\theta_0 = \theta = 0$) (13) can be simplified to

$$\|\mathbf{v}'\|_{i+1} = c\tau(\mathbf{v}'_0, c_0) + \sqrt{e'^2_x + (\|\mathbf{v}'\|_i - e'_z)^2}. \tag{16}$$

F. MEAN VIRTUAL SOURCE POSITION

After all the virtual source positions have been estimated numerically using FPI for elements in the active aperture, one singular virtual source position is calculated by taking the mean value

$$\|\mathbf{v}'\| = \frac{1}{N}\sum_{n=1}^{N}\|\mathbf{v}(\mathbf{e}'(n)\|, \tag{17}$$

where $\mathbf{v}(\mathbf{e}'(n)$ is the estimated virtual source position as a function of the n'th element position and N is the number of elements. We assume here that the elements have the same size and, consequently, (17) is a sum without weighting.

An example of what is averaged in (17) is illustrated in Fig. 5. The illustration in Fig. 5 shows only two of the N estimates averaged together in (17). The final position of the virtual source in the original coordinate system is then found by

$$\mathbf{v} = R(-\theta_\rho) \times \begin{pmatrix} \|\mathbf{v}'\|\sin\theta \\ 0 \\ \|\mathbf{v}'\|\cos\theta \end{pmatrix} + \mathbf{o}. \tag{18}$$

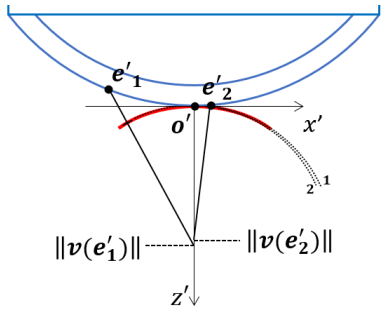

FIGURE 5. Example of two virtual source depth solutions for different element positions $\mathbf{e_1}'$ and $\mathbf{e_2}'$ in the active transmit aperture. The solid red line is the distorted transmit delay and is not a perfect circle, but can be approximated piece-wise as circles with a defined center, *i.e.* multiple virtual source estimates. The black dotted arcs show the circular curvatures for the two virtual sources. Both arcs intersect the transmit origin o′.

This results in a virtual source position that on average captures the TOF curvature caused by a focused transmission with the assumed sound speed c_0 in a medium with sound speed c.

III. METHOD

In order to validate the theory for the virtual source correction given in Section II, we first conduct a simulation study of transmit flight times (TOF), and secondly we perform a focusing quality evaluation study in a controlled setting. The two studies investigate a medium with a sound speed of 1540 m/s and assume different sound speeds when transmitting the focused pulse sequence.

A. FIXED POINT ITERATION (FPI)

The virtual source depths are solved using the Fixed Point Iteration (FPI) method described in Section II-E. Elements with F-number larger than 20, *i.e.* $20\|\mathbf{e}' - \mathbf{o}'\| < \|\mathbf{v}' - \mathbf{o}'\|$, are excluded from the calculation. The exclusion is done because the estimates for elements with large F-numbers converge very slowly in the FPI due to the almost straight/plane transmit delay. Including these elements has negligible effect on the mean estimated virtual source depth. The FPI is initialized with $\|\mathbf{v}'\|_{i=0} = \frac{c_0}{c}\|\mathbf{v_0}'\|$ and terminates when the difference between successive virtual source depth estimates is less than 100 nm ($|\|\mathbf{v}'\|_{i=j} - \|\mathbf{v}'\|_{i=j-1}| < 100\text{nm}$).

$$\tau(\mathbf{v}'_0, c_0) = \frac{\|\mathbf{v}'\| - \sqrt{\left(\|\mathbf{v}'\|\frac{c}{c_0}\sin(\theta_0) - e'_x\right)^2 + \left(\|\mathbf{v}'\|\sqrt{1 - \left(\frac{c}{c_0}\sin(\theta_0)\right)^2} - e'_z\right)^2}}{c}, \tag{12}$$

$$\|\mathbf{v}'\|_{i+1} = c\tau(\mathbf{v}'_0, c_0) + \sqrt{\left(\|\mathbf{v}'\|_i\frac{c}{c_0}\sin(\theta_0) - e'_x\right)^2 + \left(\|\mathbf{v}'\|_i\sqrt{1 - \left(\frac{c}{c_0}\sin(\theta_0)\right)^2} - e'_z\right)^2}\,. \tag{13}$$

TABLE 1. K-wave simulation setup for TOF simulations of a phased array with focused transmission

Parameter	Value	Units
Array geometry	Linear phased	-
Array ROC	Inf. (Flat)	mm
Active aperture length	19.2	mm
Array pitch	0.2	mm
Number of elements	96	-
Pulse	Gaussian 2-cycles	-
Center frequency	2	MHz
Grid spacing	0.1	mm
Grid dimension	2048×2048	pixels
Medium speed of sound	1540	m/s
Medium density	1020	kg/m^3
K-wave CFL number	0.5	-
Focus depths	19.2, 38.4, 75.8, 153.6	mm
Steering angle	30	degrees

TABLE 2. K-wave simulation setup for TOF simulations of curvilinear array with focused transmission

Parameter	Value	Units
Array geometry	Curvilinear	-
Array ROC	20	mm
Active aperture length	19	mm
Array pitch	0.2	mm
Number of elements	96	-
Pulse	Gaussian 2-cycles	-
Center frequency	2	MHz
Grid spacing	0.1	mm
Grid dimension	256×4096	pixels
Medium speed of sound	1540	m/s
Medium density	1020	kg/m^3
K-wave CFL number	0.5	-
Focus depths	19, 38, 76, 150	mm
Steering angle	0	degrees

B. K-WAVE TIME-OF-FLIGHT

The TOF from focused transmits with different F-numbers and different deviations of the speed of sound in the medium are computed using the k-Wave ultrasound simulator [28]. The TOFs are found by simulating a propagating pressure wave and evaluating the first time in which the pressure value of each pixel is between 0 and −18dB normalized to the simulation maximum pressure ($20\log_{10}(p_{\max})$).

A curvilinear array without steering, described in Table 2, and a flat phased array with steering, described in Table 1, are simulated. The virtual source locations are estimated using (16) for the curvilinear array and (14) for the phased array. Virtual source positions are computed for each transducer element in the arrays and averaged according to (17).

The resulting TOFs simulations are visualized using contour plots in Section IV-A. Contour plots are chosen because they visualize the curvature of the TOF, which is what is modeled by a virtual source.

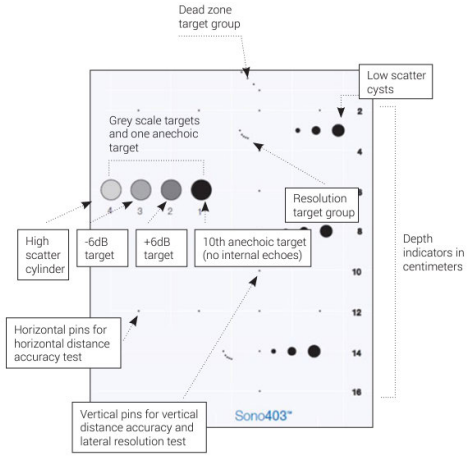

FIGURE 6. Gammex multi-purpose phantom Sono403. Original image from [29].

The virtual source estimate with the highest depth change in Section IV-A is the case $c_0 = 1640$ m/s in Fig. 8c, with the estimated focus depth being 110 mm and the assumed depth being 75 mm. To further investigate this estimate, a transmission with focus at 110 mm without sound speed error ($c_0 = c_m = 1540$ m/s) is simulated.

C. IN VITRO IMAGE QUALITY EVALUATION

Two experimental data acquisitions setups are conducted using a Vivid E95 (GE Vingmed Ultrasound AS, Horten Norway) scanner. The scanner supports the storage of the received channel data prior to receive beamforming. The first setup is an acquisition using a 1D linear phased array probe and a Gammex Sono403 phantom (Sun Nuclear, Asbury Ave) [29]. The structures of this phantom are visualized in Fig. 6. The second is an acquisition with a 1D curvilinear probe and the same Gammex Sono403 phantom. The setup details are provided in Table 3 and Table 4.

A channel data set is recorded assuming a speed-of-sound of 1640 m/s on Tx. The dataset is Rx beamformed using the beamformer in (6), implemented in the UltraSound ToolBox [17]. Three images are beamformed with the following beamforming settings:

1) Uncorrected (UC): Assuming 1640 m/s on both Tx and Rx
   - This setting performs DRF and RTB with wrong sound speed and virtual source position.
2) Naive Correction (NC): Assuming 1640 m/s on Tx, 1540 m/s on Rx, but not correcting the virtual source position.
   - This setting use correct sound speed for DRF but wrong virtual source position for RTB.
3) Virtual Source Corrected (CVS): Assuming 1640 m/s on Tx, 1540 m/s on Rx and correcting the virtual source position.

TABLE 3. Settings and parameters for *in vitro* channel data acquisition and beamforming with C1-6

Parameter	Value	Units
System	E95	-
Transducer array	GE C1-6-D	-
Array geometry	1D Curvilinear	-
Array length	67.2	mm
Array elements	192	MHz
Azimuth ROC	56	mm
Frequency	2.0 / 4.0	MHz
Transmit aperture length	22.75	mm
Focus depth	81.1	mm
Tx F-Number	3.56	-
Scan angle	65	degrees
Number of transmit events	88	-
Phantom	Sono403	-
Medium sound speed	1540	m/s
USTB Tx F-Number	4	-
Min. Tx beam width ($W_{\min}$)	6	mm
USTB Rx F-Number	1	-

TABLE 4. Settings and parameters for *in vitro* channel data acquisition and beamforming with 6S-D

Parameter	Value	Units
System	E95	-
Transducer array	GE 6S-D	-
Array geometry	1D Phased array	-
Array length	15.36	mm
Azimuth ROC	Inf. (Flat)	mm
Array elements	96	
Frequency	3.9	MHz
Transmit aperture length	15.36	mm
Focus depth	75.6	mm
Transmit F-Number	4.92	-
Scan angle	80	degrees
Number of transmit events	96	-
Phantom	Sono403	-
Medium sound speed	1540	m/s
USTB Tx F-Number	5	-
Min. Tx beam width ($W_{\min}$)	7.6	mm
USTB Rx F-Number	1	-

- This setting use correct DRF and correct virtual source position for RTB. The virtual source position is estimated using the theory in Section II.

The three images are beamformed into the effective scan grid described in Section II-A. Setting (c) uses the corrected virtual source position found using (14) and (16) for the phased array and the curvilinear case, respectively.

The RTB implementation in the USTB provides a method for masking which pixels are coherently compounded over multiple transmit events. This is called the geometric mask, wave apodization, or RTB weighting, and models the beam

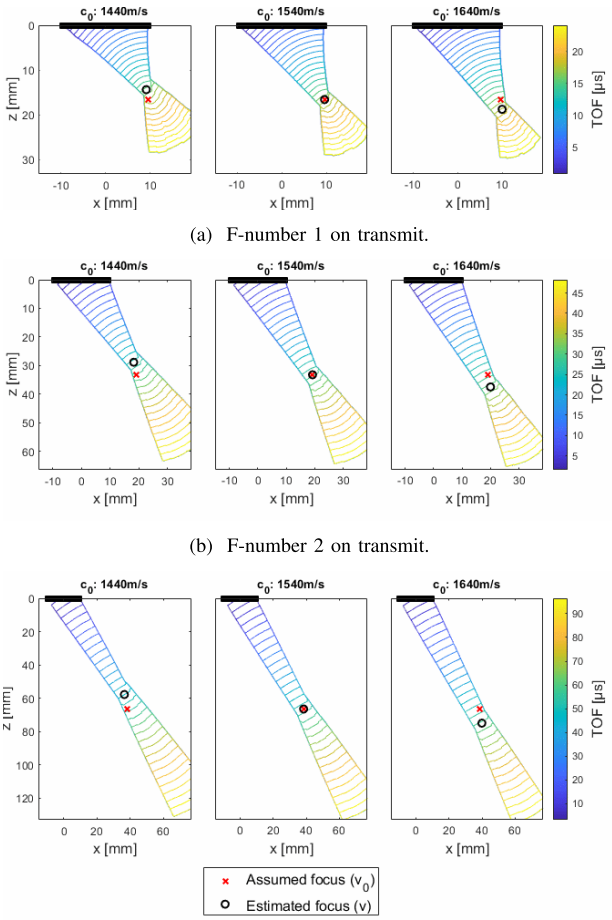

(a) F-number 1 on transmit.

(b) F-number 2 on transmit.

(c) F-number 4 on transmit.

FIGURE 7. Transmit flight time (TOF) from the transmitted steered and focused wavefront from the phased array transducer in medium with 1540 m/s and assuming a different speed of sound c_0 during Tx beamforming. The assumed focus v_0 is used to set the aperture delay $\tau(v_0, c_0)$. The estimated focus is the virtual source position v found by solving the equations in (9)-(18).

profile of each transmit event. USTB settings are given in Table 4 and Table 3. The *in vitro* images are beamformed using the unified virtual source delay model, which uses (5) to calculate the TOF inside the geometric beam mask and an interpolated TOF outside the mask [30].

We investigate the resolution of the different beamformer settings by evaluating lateral intensity plots through a point scatter in the Gammex phantom. The resolution of the point targets is quantified by the full-width opening angle at −12dB referenced to the peak. The width is measured in degrees. To be able to determine the angle axis, we need to assume a speed of sound. Here, we assume that the sound speed is 1540 m/s, which is the true sound speed in the phantom.

IV. RESULTS

A. SIMULATION of TRANSMIT TOFs in K-WAVE

Contours of the simulated TOFs using the phased array, described in Table 2, are visualized in Fig. 7. The focus position used to set up the pulse sequence delays is plotted as

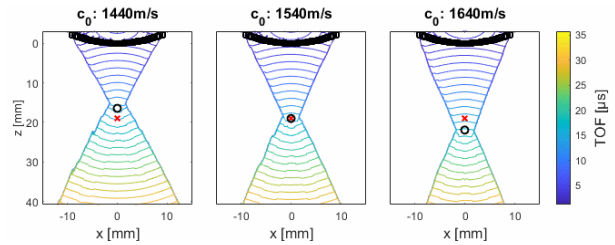

(a) F-number 1 on transmit

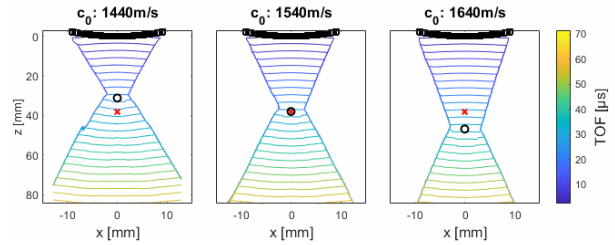

(b) F-number 2 on transmit

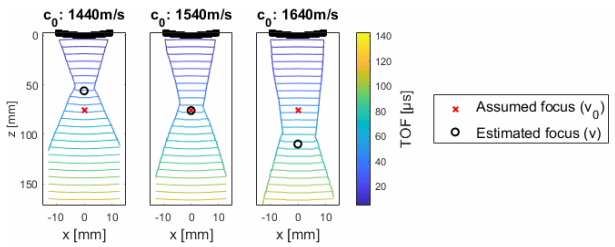

(c) F-number 4 on transmit

FIGURE 8. Transmit flight time (TOF) from focused transmits from a curvilinear array in a medium with 1540 m/s and different sound speeds c_0 assumed during Tx beamforming. The assumed focus v_0 is used to set the aperture delay $\tau(v_0, c_0)$. The estimated focus is the virtual source position v found by solving the equations in (9)-(18).

a red cross. Our estimated focus depth calculated from (18) in Section II is plotted as a black circle. Similarly, contours of the simulated TOFs using the curvilinear array, described in Table 2, are visualized in Fig. 8. Same notation is used for the focus positions as in Fig. 7.

The case $c_0 = 1640$ m/s in Fig. 8c, with the estimated focus depth being 110 mm and the assumed depth being 75 mm is further investigated by also simulating a transmitted wave with the 110 mm focus depth and the correct sound speed assumption ($c_0 = c_m = 1540$ m/s). The similarity between the two TOF simulations is shown in Fig. 9.

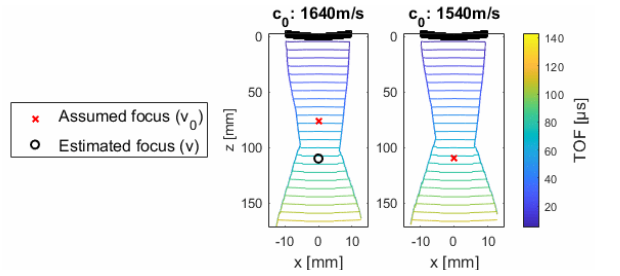

FIGURE 9. Comparison of simulated TOFs. The figure on the left is the TOF with F-number 4 ($\|v_0\| = 75$mm) and estimated depth $\|v\| = 110$mm due to sound speed error (the same as in Fig. 8c). The rightmost figure is the simulated TOF where the assumed focus depth is $\|v_0\| = 110$mm and using correct sound speed. The different assumed foci v_0 are used to set the aperture delay $\tau(v_0, c_0)$. The estimated focus in the left figure is the virtual source position v found by solving the equations in (9)-(18).

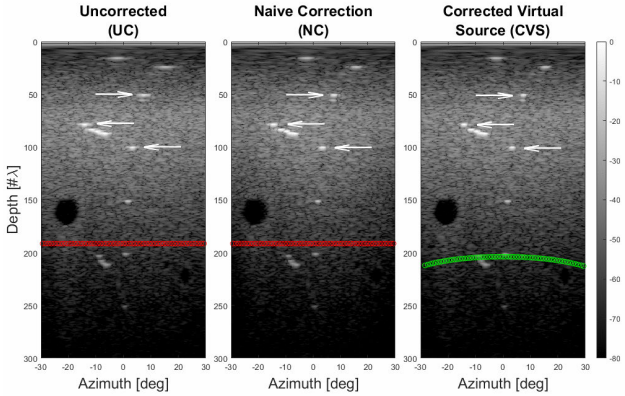

FIGURE 10. Beamspace images of Gammex phantom with the 6S phased array probe and beamformed with settings described in Section III-C. Arrows indicate the PSFs in Fig. 11. The transmit focus points used in the Rx beamforming are plotted in red and green. Red is the assumed focus position (virtual source) and green is the estimated.

B. IN VITRO IMAGE QUALITY EVALUATION

The figures in the following section use the three beamforming settings Uncorrected (UC), Naive Correction (NC) and Corrected Virtual Source (CVS) described in Section III-C. The settings use the same channel data with the sound speed 1640 m/s assumed on transmit with the medium sound speed of 1540 m/s.

1) LINEAR PHASED ARRAY

Fig. 10 shows the three beamformed images of the Gammex phantom in Fig. 6 using the GE 6S phased array probe described in Table 4. The images are shown in beamspace with log-compression ($20\log_{10}|\cdot|$) applied before visualization.

The difference in resolution between the beamforming settings for the phased array is shown by the lateral lines through the point scatters in Fig. 11. Point scatters are indicated by an arrow in Fig. 10. It is evident that the beamforming setting with Corrected Virtual Source (CVS) has better resolution compared to the two settings with an error in the speed-of-sound (UC) and an error in virtual source position (NC). Table 5 quantifies the PSFs with full-width values of -12dB of the peak value.

2) CURVILINEAR ARRAY

Fig. 12 shows the three beamformed images of a phantom captured with the GE C1-6 curvilinear array probe, described in Table 3. Fig. 13 and Table 6 show the resolution measurements of the target points in the phantom. Table 6 quantifies the PSFs with the -12dB opening angle as

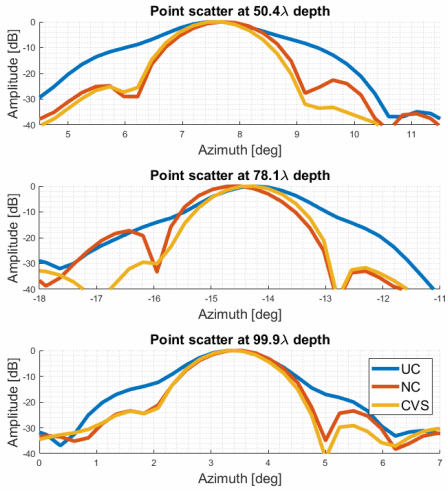

FIGURE 11. PSFs of phased array beamforming setups with different speed of sounds and virtual source positions. The PSFs are normalized to their individual maxima.

TABLE 5. PSF width (-12dB) resolution measures of phased array beamforming setups with different speed-of-sounds and different virtual source locations seen in Fig. 10

	Uncorrected (UC)	Naive Correction (NC)	Corrected Virtual Source (CVS)
50.4λ	4.12°	2.29°	2.21°
78.1λ	3.06°	2.29°	2.21°
99.9λ	2.67°	2.25°	2.15°

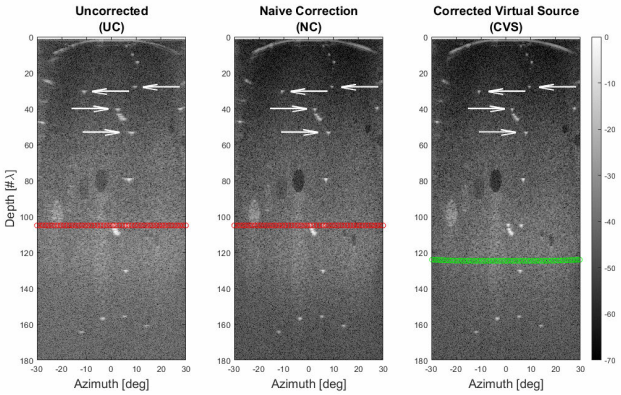

FIGURE 12. Beamspace images of Gammex phantom with cysts, speckle and point targets. Imaged with the C1-6 curvilinear probe and beamformed with the settings described in Section III-C. Arrows indicate the depth of the cross section in Fig. 13. The transmit focus points used in Rx beamforming are plotted red and green. Red is the assumed focus position (virtual source) and green is the estimated.

described in Section III-C. The values indicate that the correction of virtual source improves the resolution of point scatters by retrospectively correcting the sound speed. A marked improvement in resolution is caused by performing a naive sound speed correction, but this is further improved by correcting the virtual source position.

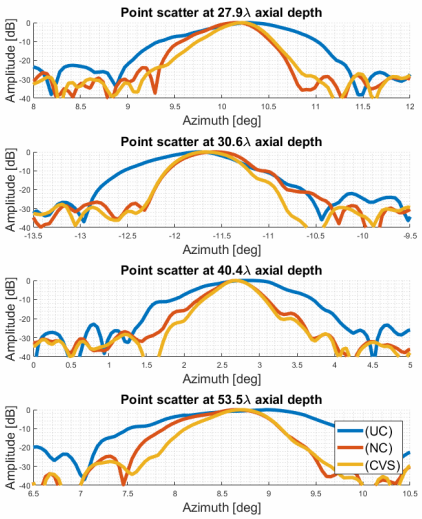

FIGURE 13. PSFs of curvilinear array beamforming setups with different speed of sounds and virtual source positions seen in Fig. 12. The PSFs are normalized to each individual maximum.

TABLE 6. PSF width (−12dB) resolution measures of curvilinear array beamforming setups with different speed-of-sounds and different virtual source locations seen in Fig. 13

	Uncorrected (UC)	Naive Correction (NC)	Corrected Virtual Source (CVS)
27.9λ	1.81°	1.06°	0.91°
30.6λ	1.65°	1.17°	0.94°
40.5λ	2.16°	1.03°	0.91°
53.5λ	2.39°	1.34°	1.11°

V. DISCUSSION

The TOF contour simulations from k-wave in Fig. 7 and Fig. 8 shows expected beam geometry with converging contours before the focus point and diverging contours after focus. The estimated angle of the virtual sources in Fig. 7 seems to steer along the refracted beam angle for all assumptions in sound speed and for all F-numbers. As expected, we see that the TOF curvature becomes flatter for higher F-numbers. The estimated depths for virtual source positions are reasonable in relation to the simulated TOF contours. The estimate with $c_0 = 1640$ m / s and F-number 4 appears at first to be deeper than what is true. However, the investigation of this setting in Fig. 9 shows a clear similarity between the two contours. This supports the validity of the method.

The uncorrected beamforming setting using 1640 m/s on both Tx and Rx is generally the setting with the worst measured resolution, as expected. The measured resolution is improved by naively correcting the sound speed and is even further improved by also correcting the virtual source for RTB. *I.e.* the proposed CVS method seems to increase focus quality over UC and NC.

The PSF sidelobe levels of the uncorrected and naive sound speed correction methods, seen in Fig. 11 and Fig. 13,

appear to be higher than the levels of the CVS correction method. The sidelobe levels are below −12dB and are not measured by the resolution measurements in Table 5 and Table 6.

It is also evident from Fig. 11 that there is a skewed scatter artifact seen in Fig. 11 and in particular for the 78.1λ depth. The naive beamforming setting assumes a wave propagation in one direction for the transmit beam and assumes a different direction on the wave propagation for the receive beam because it does not compensate the virtual source. Such a steering miss-match will result in nonsymmetric sidelobe level because the product of transmit and receive beam profiles will multiply the mainlobe with a sidelobe. The PSF in Fig. 11 can be viewed as a two-way transverse beam profile in focus, and display this skewed PSF. This skewness is not measured using the resolution measurements in Table 5.

The resolution improvement seen by correcting the virtual source in addition to correcting the sound speed is shown by comparing the NC and CVS resolution measurements. The results in Table 5 and Table 6 suggest that the resolution in the curvilinear case improves more from the virtual source correction than in the phased array case. This is expected because the curvilinear case has an additional delay term for the ROC curvature that contributes to the synthetic focusing. Secondly, the transmit F-number for the phased array case is higher, with F-number 5, compared to 3.6 for the curvilinear case.

Virtual source depth correction of higher F-number transmissions has less effect on the synthetic focusing than for lower F-numbers because the TOF curvature will be less changed at higher depths. The curvature of a circle is inversely proportional to its radius, and the change of TOF curvature as a function of depth is therefore inversely proportional to depth squared ($\|\mathbf{v}'\|^{-2}$). This is similar to how a spherical wave approximates a plane wave at a sufficiently long distance from the spherical origin. The number of numerical iterations needed to converge with FPI will, as a consequence, increase with an increased F-number. For sufficiently high F-numbers and limited computational resources, the Fraunhofer correction in (15) can be used as an approximate.

The proposed method for virtual source correction assumes knowledge of the sound speed prior to and after the refraction at the array boundary. However, the method can also consider refraction at other boundaries in the imaging medium, if the sound speeds and the boundary position are known. A potential method for calculating the transmit TOF for a distributed sound speed map can be to iterate through the contours of the map and estimate a new virtual source for each contour boundary. The study of the virtual source model for distributed sound speed and phase aberrations is an interesting topic for future work.

VI. CONCLUSION

A general theory for receive scan grid and virtual source correction has been derived for retrospective sound speed change and pixel-to-pixel image quality comparison. The theory has been demonstrated in the cases of 1D phased and curvilinear arrays *in silico* and *in vitro*. The simulated wave propagation in cases with wrong sound speed assumption has been shown to have a transmit focus that matches the estimate given by our suggested equations. This estimate enables the use of synthetic transmit focusing when changing the sound speed retrospectively. Applying the correction to the virtual source during receive beamforming has been shown to improve two-way focusing and avoid image artifacts.

ACKNOWLEDGMENT

The author Anders E. Vrålstad would like to thank Kjell Kristoffersen for his scientific support and insightful discussions.

REFERENCES

[1] G. D. Ludwig, "The velocity of sound through tissues and the acoustic impedance of tissues," *J. Acoust. Soc. Amer.*, vol. 22, no. 6, pp. 862–866, Nov. 1950.

[2] H. Azhari, *Appendix A: Typical Acoustic Properties Tissues*. Hoboken, NJ, USA: Wiley, 2010, pp. 313–314.

[3] R. Ali et al., "Aberration correction in diagnostic ultrasound: A review of the prior field and current directions," *Zeitschrift Für Medizinische Physik*, vol. 33, no. 3, pp. 267–291, Aug. 2023.

[4] M. E. Anderson and G. E. Trahey, "The direct estimation of sound speed using pulse–echo ultrasound," *J. Acoust. Soc. Amer.*, vol. 104, no. 5, pp. 3099–3106, Nov. 1998.

[5] F. R. Pereira, J. C. Machado, and W. C. A. Pereira, "Ultrasonic wave speed measurement using the time-delay profile of RF-backscattered signals: Simulation and experimental results," *J. Acoust. Soc. Amer.*, vol. 111, no. 3, pp. 1445–1453, Mar. 2002.

[6] J. F. Krucker, J. B. Fowlkes, and P. L. Carson, "Sound speed estimation using automatic ultrasound image registration," *IEEE Trans. Ultrason., Ferroelectr., Freq. Controll*, vol. 51, no. 9, pp. 1095–1106, Sep. 2004.

[7] C. Yoon, Y. Lee, J. H. Chang, T.-K. Song, and Y. Yoo, "In vitro estimation of mean sound speed based on minimum average phase variance in medical ultrasound imaging," *Ultrasonics*, vol. 51, no. 7, pp. 795–802, Oct. 2011.

[8] M. Imbault et al., "Robust sound speed estimation for ultrasound-based hepatic steatosis assessment," *Phys. Med. Biol.*, vol. 62, no. 9, pp. 3582–3598, May 2017.

[9] D. Napolitano et al., "Sound speed correction in ultrasound imaging," *Ultrasonics*, vol. 44, pp. e43–e46, Dec. 2006.

[10] A. Benjamin et al., "Surgery for obesity and related diseases: I. A novel approach to the quantification of the longitudinal speed of sound and its potential for tissue characterization," *Ultrasound Med. Biol.*, vol. 44, no. 12, pp. 2739–2748, Dec. 2018.

[11] R. Ali et al., "Local sound speed estimation for pulse-echo ultrasound in layered media," *IEEE Trans. Ultrason., Ferroelectr., Freq. Control*, vol. 69, no. 2, pp. 500–511, Feb. 2022.

[12] W. Simson, L. Zhuang, S. J. Sanabria, N. Antil, J. J. Dahl, and D. Hyun, "Differentiable beamforming for ultrasound autofocusing," in *Home Medical Image Computing and Computer Assisted Intervention—MICCAI*. Cham, Switzerland: Springer, 2023, pp. 428–437.

[13] H. Strohm, V. Kuhlen, J. Jenne, M. Günther, and S. Rothlübbers, "Effect of geometric and transmit corrections on global speed of sound estimation," in *Proc. IEEE Int. Ultrason. Symp. (IUS)*, Oct. 2022, pp. 1–4.

[14] C. H. Frazier and W. D. O'Brien, "Synthetic aperture techniques with a virtual source element," *IEEE Trans. Ultrason., Ferroelectr., Freq. Control*, vol. 45, no. 1, pp. 196–207, Jan. 1998.

[15] M.-H. Bae and M.-K. Jeong, "A study of synthetic-aperture imaging with virtual source elements in B-mode ultrasound imaging systems," *IEEE Trans. Ultrason., Ferroelectr., Freq. Control*, vol. 47, no. 6, pp. 1510–1519, Nov. 2000.

[16] C. Passmann and H. Ermert, "A 100-MHz ultrasound imaging system for dermatologic and ophthalmologic diagnostics," *IEEE Trans. Ultrason., Ferroelectr., Freq. Control*, vol. 43, no. 4, pp. 545–552, Jul. 1996.

[17] A. Rodriguez-Molares et al., "The ultrasound tool box," in *Proc. IEEE Int. Ultrason. Symp. (IUS)*, Sep. 2017, pp. 1–4.

[18] S. I. Nikolov, J. Kortbek, and J. A. Jensen, "Practical applications of synthetic aperture imaging," in *Proc. IEEE Int. Ultrason. Symp.*, Oct. 2010, pp. 350–358.
[19] L. Mo, "A retrospective look at retrospective transmit beamforming," in *Proc. IEEE Int. Ultrason. Symp. (IUS)*, Sep. 2020, pp. 1–4.
[20] N. Bottenus, "Recovery of the complete data set from focused transmit beams," *IEEE Trans. Ultrason., Ferroelectr., Freq. Control*, vol. 65, no. 1, pp. 30–38, Jan. 2018.
[21] R. Ali, C. D. Herickhoff, D. Hyun, J. J. Dahl, and N. Bottenus, "Extending retrospective encoding for robust recovery of the multistatic data set," *IEEE Trans. Ultrason., Ferroelectr., Freq. Control*, vol. 67, no. 5, pp. 943–956, May 2020.
[22] N. Bottenus, "Comparison of virtual source synthetic aperture beamforming with an element-based model," *J. Acoust. Soc. Amer.*, vol. 143, no. 5, pp. 2801–2812, May 2018.
[23] R. Mallart and M. Fink, "Adaptive focusing in scattering media through sound-speed inhomogeneities: The van Cittert Zernike approach and focusing criterion," *J. Acoust. Soc. Amer.*, vol. 96, no. 6, pp. 3721–3732, Dec. 1994.
[24] B. A. Angelsen, *Waves, Signals and Signal Processing in Medical Ultrasonics*, vol. 2. Trondheim, Norway: Department of Physiology and Biomedical Engineering, Norwegian University of Science and Technology, 1996.
[25] C.-H. Chang, Y.-F. Chang, Y. Ma, and K. K. Shung, "Reliable estimation of virtual source position for SAFT imaging," *IEEE Trans. Ultrason., Ferroelectr., Freq. Control*, vol. 60, no. 2, pp. 356–363, Jan. 2013.
[26] I. Jacques and C. Judd, "Linear algebraic equations," in *Numerical Analysis*. Cham, Switzerland: Springer, 1997, pp. 8–42.
[27] Q. Chen and J. A. Zagzebski, "Simulation study of effects of speed of sound and attenuation on ultrasound lateral resolution," *Ultrasound Med. Biol.*, vol. 30, no. 10, pp. 1297–1306, Oct. 2004.
[28] E. Martin, Y. T. Ling, and B. E. Treeby, "Simulating focused ultrasound transducers using discrete sources on regular Cartesian grids," *IEEE Trans. Ultrason., Ferroelectr., Freq. Control*, vol. 63, no. 10, pp. 1535–1542, Oct. 2016.
[29] J. A. Zagzebski. *Sono403 Multi-Purpose Phantoms*. Accessed: Jan. 25, 2023. [Online]. Available: https://www.sunnuclear.com/uploads/documents/datasheets/Diagnostic/Sono403-Ultrasound111920.pdf
[30] N. Q. Nguyen and R. W. Prager, "High-resolution ultrasound imaging with unified pixel-based beamforming," *IEEE Trans. Med. Imag.*, vol. 35, no. 1, pp. 98–108, Jan. 2016.

ANDERS EMIL VRÅLSTAD (Graduate Student Member, IEEE) was born in Oslo, Norway, in 1997. He received the M.Sc. degree in electronic engineering and acoustics from the Norwegian University of Science and Technology (NTNU), where he is currently pursuing the Ph.D. degree in medical ultrasound beamforming, speed of sound, and machine learning with the Department of Circulation and Medical Imaging.

His current research interests include ultrasound beamforming, aberration correction, and image quality enhancement.

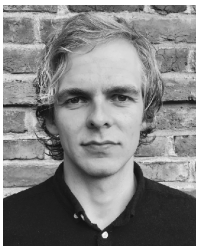

OLE MARIUS HOEL RINDAL (Member, IEEE) was born in Hamar, Norway, in 1990. He received the M.S. degree in computer science (signal processing) from the University of Oslo (UiO), Norway, in 2014, and the Ph.D. degree, in 2019. His Ph.D. dissertation entitled Software Beamforming in Medical Ultrasound Imaging-A Blessing and a Curse. He is currently a Senior Lecturer with UiO as well as the Co-Founder and Technology Manager of the company Sonair AS. His research interests include signal processing, beamforming, medical image formation, image processing, and machine learning, as well as physiological and biomechanical aspects of cross-country skiing.

TORE GRÜNER BJÅSTAD (Member, IEEE) was born in Lesund, Norway, in 1977. He received the sivil ingenioer (M.Sc.) degree in electronics and telecommunications from the Norwegian University of Science and Technology (NTNU), Trondheim, Norway, in 2002, and the Ph.D. degree from the Department of Circulation and Medical Imaging, Faculty of Medicine, NTNU, in 2009. He is currently with GE Healthcare, GE Vingmed Ultrasound AS, Horten, Norway. His main research interests include beamforming and signal processing methods for improved ultrasound image quality.

SVEIN-ERIK MÅSØY was born in Halden, Norway, in 1975. He received the M.Sc. and Ph.D. degrees in applied mechanics, thermodynamics, and fluid dynamics from the Norwegian University of Science and Technology (NTNU), Trondheim, Norway, in 1999 and 2004, respectively. His Ph.D. dissertation entitled Estimation and Correction of Aberration in Medical Ultrasound Imaging.

He is currently an Associate Professor with the Department of Circulation and Medical Imaging, NTNU. His current research interests include beamforming, machine learning, and non-destructive testing using ultrasound.